J. Mech. Phys. Solids 179 (2023) 105351

Contents lists available at ScienceDirect

Journal of the Mechanics and Physics of Solids

journal homepage: www.elsevier.com/locate/jmps

A semi-analytical solution to the stress intensity factors of branched cracks

Zhuo-Er Liu [a,c], Yujie Wei [a,b,c,*]

[a] LNM, Institute of Mechanics, Chinese Academy of Sciences, Beijing 100190, China
[b] Eastern Institute for Advanced Study (EIAS), Ningbo, Zhejiang 315200, China
[c] School of Engineering Sciences, University of Chinese Academy of Sciences, Beijing 100049, China

ARTICLE INFO

Keywords:
Crack branching
Stress intensity factors
Conformal mapping
Fracture mechanics

ABSTRACT

Crack branching is ubiquitous in engineering practice, and it often takes place when a crack is subjected to dynamic stress fields, or runs into heterogeneous regions. The mechanical analysis of branched cracks is of great significance in safety analysis and crack-path engineering. In this work we developed a theoretical method to calculate the stress intensity factors (SIFs) of branched cracks. By employing both Schwarz–Christoffel mapping and Muskhelishvili approach, we present an asymptotic approximation for the conformal mapping and SIFs of arbitrary branched cracks are then readily derived. We further demonstrate the convenience of this analytical approach to obtain the SIFs of forked crack as well as four-branched cracks. The theoretical solutions are validated by using finite-element simulations. It is shown that the semi-analytical approach agrees well with the FEM calculations on SIFs. The analytical methods supply a general way to solve the SIFs and therefore the energy release rate of branched cracks. It can then be adopted to understand crack splitting and crack network engineering.

1. Introduction

When cracks are subjected to dynamic or non-uniform stress fields, or propagate in heterogeneous media, they often kink or branch. This phenomenon is widely observed in engineering practice, and has received lots of attention for its significance in predicting crack propagation.

In order to understand the propagation of a branched crack, stress intensity factors (SIFs) of the crack-tip are often desired (Irwin, 1957; Hutchinson et al., 1987). Once the SIFs are obtained, one may adopt the energy release rate criterion to predict the propagation path (Hussain et al., 1973; He and Hutchinson, 1989; He et al., 1991). Therefore, finding a way to accurately calculate the SIFs has become a core subject in fracture mechanics, and has received wide interests from researchers of the solid mechanics community (Williams, 1957; Andersson, 1969; Rice, 1972; Chatterjee, 1975; Cotterell and Rice, 1980; Hayashi and Nemat-Nasser, 1981; Amestoy and Leblond, 1992; Salvadori and Fantoni, 2016; Leblond et al., 2019).

Dated back to 1960s, Andersson (1969) developed a method to calculate the SIFs of branched cracks by using complex variable functions, but it was found later on that the formula neglecting the discontinuity of the complex variable functions. A simplified version of branched cracks with only two segments (kinked cracks) was then explored intensively. One attempt is to use the combination of the SIFs of the main crack to represent the SIFs of the kink (Bilby and Cardew, 1975; Bilby et al., 1977). Lo (1978) gave an integral equation to solve the SIFs of a kinked crack by regarding a crack as continuous distribution of dislocations. Cotterell and Rice (1980) adopted a perturbation method to calculate the SIFs of a slightly curved or kinked crack. Karihaloo et al. (1981)

* Corresponding author at: LNM, Institute of Mechanics, Chinese Academy of Sciences, Beijing 100190, China.
E-mail address: yujie_wei@lnm.imech.ac.cn (Y. Wei).

https://doi.org/10.1016/j.jmps.2023.105351
Received 8 March 2023; Received in revised form 21 May 2023; Accepted 6 June 2023
Available online 15 June 2023

extended this perturbation method by using two-order asymptotic expansions. Sumi et al. (1983) employed the same strategy to solve the crack kinking problem in a finite body. Along this track, He et al. (1991) gave an expression of the SIFs of cracks with small kinks by incorporating the influence of T-stress. Chen et al. (2009) carried out an asymptotic solution of the SIFs and T-stress of kinked cracks with infinitesimal kink length by using singular integral equation method. Those perturbation methods often work well for very short kinks relative to their original ones. The SIFs of kinked crack with an arbitrary sized was first solved by Chatterjee (1975). He numerically solved the integral equation deduced from the boundary value problems through employing conformal mapping and Muskhelishvili approach. With the help of these methods, Liu and Wei (2021) established a framework to calculate the stress fields of arbitrarily sized kinked cracks theoretically. With known stress fields, SIFs are readily derived. Other than kinked crack, Wu (1978) employed conformal mapping to solve the elastic problem of Z-shaped cracks. He also gave a three-order asymptotic solution of SIFs of Z-shaped cracks with small kinking angle (Wu, 1979). A very recent effort developed by Vattré (2022), by adopting the geometrical resemblance of a forked crack array in an anisotropic media with a continuously distributed dislocation, gave the stress field of the forked crack array by using the Stroh formalism to the linear elastic theory of dislocations. The researches on quasi-static state can be further extended to fracture dynamics. Adda-Bedia (2005) employed conformal mapping to solve the SIFs and energy release rate of three-branched cracks with infinitesimal symmetrical branches subjected to general loading (mode I+II+III), and the results are used to analyze the branching instability in dynamic propagation and predict the critical speed for branching. Within this framework, Katzav et al. (2007) performed a quantitative study on the subsequent crack-path choice followed branching.

Rapid development in computing methods facilitates our understanding on crack-branching through numerical methods. Ferney et al. (1999) employed a cohesive element method based on FEM to modeling crack propagation along arbitrary paths. Buehler and Gao (2006) used massively parallel large-scale atomistic simulations to show that hyperelasticity plays a governing role in the onset of the instability at crack tips. Ruan et al. (2021) used peridynamics method to simulate the crack branching in asphalt mixtures. Zhang and Dunne (2022) used 3D crystal plasticity extended finite element method (CP-XFEM) to simulate the interaction of short fatigue cracks with grain boundary. Cheng and Zhou (2020) gave an energy based criterion for crack branching by using multidimensional space method. Hakimzadeh et al. (2022) investigated the finite deformation and branching of cracks in soft materials by using phase-field method. Recently, machine learning is introduced to solve complex mechanical problem, Liu et al. (2020) used machine learning model to analyze the fracture toughness. These methods provide new ways for engineering problems when analytical solutions are not available.

Observation from the fast crack propagation experiments shows the dynamic instability of brittle materials is related to a transition from a single crack to a branched crack (Sharon and Fineberg, 1996, 1999). Sundaram and Tippur (2016) used digital gradient sensing technique to investigate crack interaction and crack branching in the presence of dynamic loading. Crack path prediction is not only of importance in safety control, but also of significance for the formation of crack networks in applications like energy harvesting (Li et al., 2022). In composite materials with abundant interfaces, a crack crossing the interface may lead to the formation of a four-branched crack (Dönmez and Bažant, 2020). Fayyad and Lees (2017) used digital image correlation method to investigate crack branching in reinforced concrete beams. It is also well known that indentation at brittle films also leads to crack branching (Xu et al., 2003).

Regardless of the significant progress upon the characteristics of branched cracks, a general method to tackle the SIFs of branched cracks is till lacking. In this work, following the previously used conformal mapping and Muskhelishvili approach (Liu and Wei, 2021), we establish a theoretical framework to accurately calculate the SIFs of an arbitrary branched crack. We organize the content as follows: in Section 2, we state the boundary value problem (BVP) and give the asymptotic solutions by employing the conformal mapping and the Muskhelishvili approach. We demonstrate in Sections 3 and 4 how to use the general method to solve the stress-intensity factors of forked cracks and four-branched cracks, respectively, accompanied with finite-element validations. We close in Section 5 with some final remarks.

2. Formulation

In the previous research we have given the analytical solution of the stress fields to kinked cracks (Liu and Wei, 2021). In this work we focus on the crack-tip SIFs of an arbitrary branched crack in an infinite space. We consider a branched crack subjected to arbitrary stress status, as seen in Fig. 1a. For the convenience of analysis, let one of the branch be horizontal through rotating counter-clockwise the coordinate by an angle α. The stress status is characterized by two principal stresses σ_1 and σ_2, and the angle between σ_1 and the x_2-axis is characterized as β, as shown in Fig. 1b.

2.1. Conformal mapping

The fracture problem shown in Fig. 1b will be analyzed under linear elastic assumption and is two-dimensional in nature. For the completeness of the presentation, we repeat the essential steps to solve the linear elasticity of a typical fracture problem using the Muskhelishvili approach (Muskhelishvili, 1953). The stress field of a linear elastic problem can be derived from two complex functions $\Phi(z)$ and $\Psi(z)$ defined in the z-plane, with which we have the following equations associated with the planar stresses σ_x, σ_y and τ_{xy}

$$\sigma_x + \sigma_y = 4\Re[\Phi'(z)] = 2[\Phi'(z) + \overline{\Phi'(z)}] \tag{1a}$$

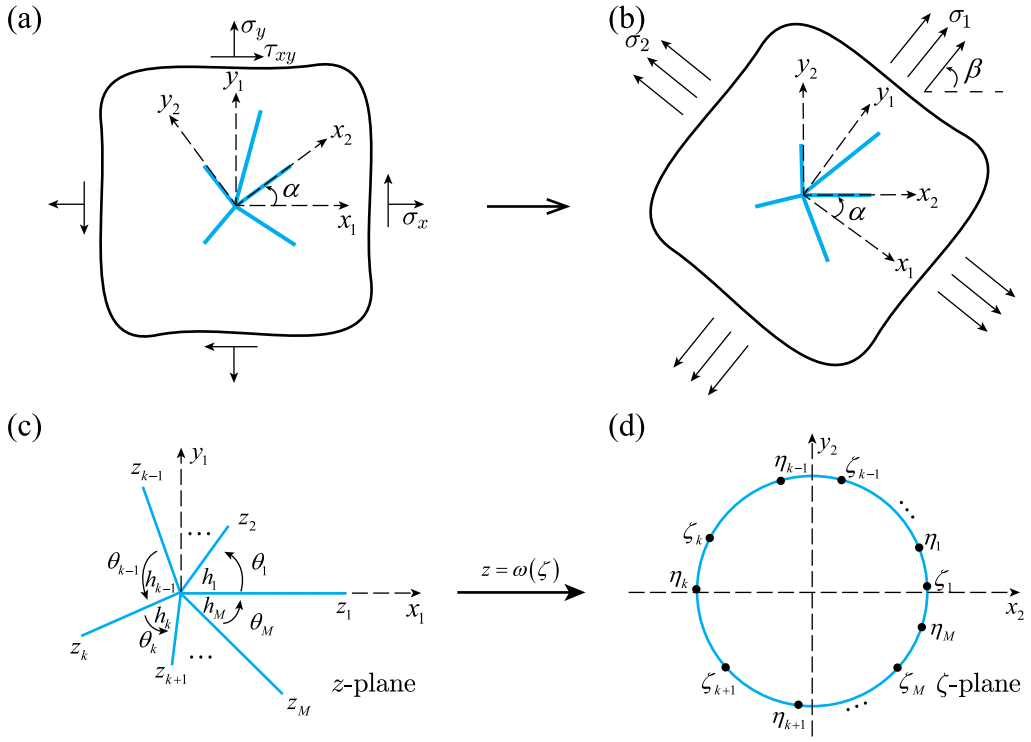

Fig. 1. The BVP of a branched crack and its conformal mapping to a unit circle. (a) A branched crack with one branch forming an angle α with respect to the x_1-axis. (b) We consider a configuration (rotating clockwise the coordinate in (a) by an angle α) so that one branch of the crack is horizontal. σ_1 and σ_2 are the principal stresses and β is the angle between σ_1 and the x_2-axis. (c) A branched crack contains M ends (from z_1 to z_M) and M joint points (from h_1 to h_M). The angle between branches k and $(k+1)$ is θ_k. (d) The mapping of these points are from ζ_1 to ζ_M and η_1 to η_M, in turn, on the unit circle.

and

$$\sigma_y - \sigma_x + 2i\tau_{xy} = 2[\overline{z}\boldsymbol{\Phi}''(z) + \boldsymbol{\Psi}'(z)] \tag{1b}$$

where $\Re(\cdot)$ denotes the real part of $(\cdot)$, $\overline{(\cdot)}$ denotes the conjugate of $(\cdot)$, $(\cdot)'$ and $(\cdot)''$ are the first and the second derivative of $(\cdot)$ with respect to z, respectively, and $z = x + iy$. The boundary condition on a general contour L is given as

$$\boldsymbol{\Phi}(t) + t\overline{\boldsymbol{\Phi}'(t)} + \overline{\boldsymbol{\Psi}(t)} = i\int_{t_0}^{t}(p_x + ip_y)ds = i[F_x(t) + iF_y(t)] = F(t) \tag{2}$$

where t_0 is a fixed point on L and t is any point on L, and (p_x, p_y) is the traction on the infinitesimal segment ds and (F_x, F_y) is the collective force exerted to the part of crack surface (from t to t_0).

Due to the complexity of possible boundary conditions, conformal mapping is usually used to simplify the above BVPs. As shown in Fig. 1c to d, we seek a transformation in the form of $z = \omega(\zeta)$, where z is a point in the z-plane and ζ is its counterpart in the ζ-plane. Usually, the boundary L in the z-plane is mapping into a unit circle in the ζ-plane. After employing the conformal mapping, we obtain the equivalent expressions of Eq. (1), which can be rewritten in terms of ζ as

$$\sigma_\rho + \sigma_\theta = 2\left[\frac{\varphi'(\zeta)}{\omega'(\zeta)} + \overline{\frac{\varphi'(\zeta)}{\omega'(\zeta)}}\right] \tag{3a}$$

and

$$\sigma_\theta - \sigma_\rho + 2\tau_{\rho\theta} = \frac{2\zeta^2}{\rho^2\overline{\omega'(\zeta)}}\left[\overline{\omega(\zeta)}\left(\frac{\varphi'(\zeta)}{\omega'(\zeta)}\right)' + \psi'(\zeta)\right] \tag{3b}$$

Here we define $\zeta = \rho e^{i\theta}$ in the ζ-plane, and $\varphi(\zeta)$ and $\psi(\zeta)$ are the counterparts of $\boldsymbol{\Phi}(z)$ and $\boldsymbol{\Psi}(z)$, and σ_ρ, σ_θ and $\sigma_{\rho\theta}$ are the radial stress, hoop stress and shear stress in the polar coordinate in the ζ-plane. Therefore, the boundary condition in Eq. (2) is rewritten as

$$\varphi(\xi) + \frac{\omega(\xi)}{\overline{\omega'(\xi)}}\overline{\varphi'(\xi)} + \overline{\psi(\xi)} = f(\xi) \tag{4}$$

where ξ is any point on the unit circle C.

We start with a general branched crack with M branches, as shown in Fig. 1c. The angle between two neighboring branches k and $k+1$ is θ_k. The length of those branches is labeled as $l_1, \dots, l_M$, in turn. As each branch has two ends, there are a total of $2M$ key points for this branched crack in the z-plane: The free ends of the M branches are referred to $z_1 = l_1, \dots, z_M = l_M e^{i\sum_{n=1}^{M-1}\theta_n}$, and those joint ends associated with each branch are labeled as $h_1, \dots, h_M$. The counterparts of these points in the ζ-plane are $\zeta_1 = e^{i\mu_1}, \dots, \zeta_M = e^{i\mu_M}$ for $z_1, \dots, z_M$, respectively, and $\eta_1 = e^{i\nu_1}, \dots, \eta_M = e^{i\nu_M}$ for $h_1, \dots, h_M$, in turn.

Schwarz–Christoffel mapping is usually employed to solve such problems where the external region of the branched crack is mapped into the outside part of a unit circle (Andersson, 1969). For the general branched crack shown in Fig. 1c, its corresponding Schwarz–Christoffel mapping function is given as

$$\omega(\zeta) = \frac{R}{\zeta}\prod_{n=1}^{M}(\zeta - \eta_n)^{\lambda_n} \tag{5}$$

where R is a real parameter and $\lambda_n = \theta_n/\pi$. There are a total of $2M+1$ real parameters in this mapping function, $\mu_1, \dots, \mu_M, \nu_1, \dots, \nu_M$, and R. These parameters can be obtained by solving the following $2M+1$ real equations (Andersson, 1969)

$$\sum_{n=1}^{M}\nu_n\lambda_n = 2\pi \tag{6a}$$

for the conservation of angles,

$$\sum_{n=1}^{M}\lambda_n \cot\left(\frac{\nu_n - \mu_k}{2}\right) = 0, \quad k = 1, 2, \dots, M \tag{6b}$$

for the constraints at the joint ends, and

$$4R\prod_{n=1}^{M}\left|\sin\left(\frac{\mu_k - \nu_n}{2}\right)\right|^{\lambda_n} = l_k, \quad k = 1, 2, \dots, M \tag{6c}$$

for the length of the M branches.

For the special case where this branched crack is of central symmetry, which means the length of each branch is equal and the angle between each branch is equal, i.e. $l_k = l$ and $\theta_k = \frac{2\pi}{M}$, $k = 1, 2, \dots, M$. The mapping function is in the form of

$$\omega(\zeta) = \frac{l}{\sqrt[M]{4}}\frac{(\zeta^M + 1)^{\frac{2}{M}}}{\zeta} \tag{7}$$

For the case of $M = 2$, the mapping function becomes a Zhukovsky function (Brown and Churchill, 2009). We further discussed the situation where $M = 3$ and $M = 4$ as examples for M being an odd and even number in Section 3 and Section 4, respectively.

However, due to the multi-value nature of the mapping function and the possible discontinuity in the term $\frac{\omega(\xi)}{\omega'(\xi)}$ in Eq. (4), it is rather difficult to employ the mapping function to solve the BVP directly, as detailed Appendix A. Alternatively, we adopt a polynomial approximation to tackle such a problem. Following this track, the mapping function in Eq. (5) can be written in Laurent series

$$\omega(\zeta) = R\left(\zeta + \sum_{n=1}^{\infty}a_n\zeta^{1-n}\right) \tag{8}$$

where a_n is the complex coefficient for the nth term in the sum. The derivative of $\omega(\zeta)$, as detailed in the Appendix B, is given as

$$\omega'(\zeta) = \omega(\zeta)\frac{\prod_{n=1}^{M}(\zeta - \zeta_n)}{\zeta\prod_{n=1}^{M}(\zeta - \eta_n)} \tag{9}$$

which may be further reformulated as

$$\omega'(\zeta)\zeta\prod_{n=1}^{M}(\zeta - \eta_n) = \omega(\zeta)\prod_{n=1}^{M}(\zeta - \zeta_n) \tag{10}$$

We now expand the product term at the left-hand-side in the above equation,

$$\prod_{n=1}^{M}(\zeta - \eta_n) = \zeta^M + \sum_{n=1}^{M}\alpha_n\zeta^{M-n} \tag{11a}$$

and that at the right-hand-side is in the form of

$$\prod_{n=1}^{M}(\zeta - \zeta_n) = \zeta^M + \sum_{n=1}^{M}\beta_n\zeta^{M-n} \tag{11b}$$

where coefficients α_n and β_n, according to Vieta theorem, are given as

$$\alpha_n = (-1)^n \sum_{1\le k_1<k_2<\cdots<k_n\le M}\eta_{k_1}\eta_{k_2}\cdots\eta_{k_n}, \quad n = 1, 2, \dots, M \tag{12a}$$

and

$$\beta_n = (-1)^n \sum_{1\le k_1<k_2<\cdots<k_n\le M} \zeta_{k_1}\zeta_{k_2}\cdots\zeta_{k_n}, \quad n = 1, 2, \ldots, M \tag{12b}$$

Then substituting Eq. (8), (11) and (12) into Eq. (10), we can obtain the recursive expression for the complex parameter a_n in the mapping function (Eq. (8)),

$$a_n = \begin{cases} 0; & n < 0 \\ 1; & n = 0 \\ \dfrac{1}{n}\displaystyle\sum_{k=1}^{M}[(k+1-n)\alpha_k - \beta_k]a_{n-k}; & n > 0 \end{cases} \tag{13}$$

However, the Laurent expansion given in Eq. (8) with a finite number of terms cannot fit the first and second order derivatives of $\omega(\zeta)$. These derivatives are quite important in solving the BVPs. Note $\omega(\zeta_k) - \omega(\zeta)$ must be the same order of $(\zeta - \zeta_k)^2$ since the image of the unit circle have a sharp tip at $\omega(\zeta_k)$. Consider the Taylor expansion of $\omega(\zeta)$ near ζ_k, we have $\omega(\zeta_k) - \omega(\zeta) = \omega'(\zeta_k)(\zeta - \zeta_k) + \omega''(\zeta_k)(\zeta - \zeta_k)^2/2$, and $\omega(\zeta)$ must respect the condition $\omega'(\zeta_k) = 0$. After enforcing the approximate expansion of $\omega(\zeta)$ to respect the exact value of $\omega''(\zeta)$ at ζ_k, we may then use this relationship for the derivation of the SIFs. To ensure the accuracy of the first and second order derivative of the expansion with a finite number of terms, the Laurent series of the mapping function need to be truncated (Bowie, 1964). We assume a truncated mapping function with $N + 2$ terms

$$\begin{aligned} \omega_T(\zeta) &= R\left[\zeta + \sum_{n=1}^{N+2} w_n \zeta^{1-n}\right] \\ &= R\left[\zeta + \sum_{n=1}^{N} a_n \zeta^{1-n} + T_1\zeta^{-N} + T_2\zeta^{-N-1}\right] \end{aligned} \tag{14}$$

where T_1 and T_2 are two additional coefficients to ensure the expansion satisfying the first and second order derivative of $(N+2)$-order Laurent series $\omega_T(\zeta)$ equal to the corresponding derivative of the exact mapping function $\omega(\zeta)$, that is

$$\omega_T'(\zeta) = R\left[1 + \sum_{n=1}^{N}(1-n)a_n\zeta^{-n} - NT_1\zeta^{-N-1} - (N+1)T_2\zeta^{-N-2}\right] = \omega'(\zeta) \tag{15a}$$

and

$$\omega_T''(\zeta) = R\left[\sum_{n=1}^{N} n(n-1)a_n\zeta^{-n-1} + N(N+1)T_1\zeta^{-N-2} + (N+1)(N+2)T_2\zeta^{-N-3}\right] = \omega''(\zeta) \tag{15b}$$

Specially, for $\omega'(\zeta)$ and $\omega''(\zeta)$ at the mapping points ζ_k (the tips of the branched crack), we have

$$\omega'(\zeta_k) = 0; \quad k = 1, 2, \ldots, M \tag{16a}$$

and

$$\omega''(\zeta_k) = \omega(\zeta_k)\frac{\prod_{n=1,n\neq k}^{N}(\zeta_k - \zeta_n)}{\zeta_k\prod_{n=1}^{N}(\zeta_k - \eta_n)}; \quad k = 1, 2, \ldots, M \tag{16b}$$

Note both T_1 and T_2 are tip-specific. We solve these two numbers for each free end of a crack branch by using the two conditions in Eq. (15). The truncated expansion of the mapping function $\omega_T(\zeta)$ we solve here does not describe the exact asymptotic behavior of $\omega(\zeta)$ near the points η_k. Since we are interested in the SIFs of the crack tips, which are connected to the asymptotic behavior near the points ζ_k, this treatment will not influence the accuracy of the results. With known $\omega_T(\zeta)$, we proceed in the next section to elaborate the procedures for solving particular BVPs.

2.2. Boundary value problem

For linear elastic and plane-deformation problems, the single valued displacement allows us to write the complex functions $\varphi(\zeta)$ and $\psi(\zeta)$ (Muskhelishvili, 1953) in the form of

$$\varphi(\zeta) = -\frac{F_x + iF_y}{2\pi(1+\kappa)}\ln\zeta + \Gamma_1 R\zeta + \sum_{n=1}^{\infty} p_n\zeta^{1-n} \tag{17a}$$

and

$$\psi(\zeta) = \frac{\kappa(F_x - iF_y)}{2\pi(1+\kappa)}\ln\zeta + \Gamma_2 R\zeta + \sum_{n=1}^{\infty} q_n\zeta^{1-n} \tag{17b}$$

where F_x and F_y are the surface tractions along the $x-$ and $y-$axes. $\Gamma_1 = \frac{1}{4}(\sigma_1 + \sigma_2)$ and $\Gamma_2 = -\frac{1}{2}(\sigma_1 - \sigma_2)e^{-2i\beta}$ are two complex coefficients that describe the loading, and σ_1 and σ_2 are the principal stresses and β is the angle between σ_1 and the x_2-axis. The material constant κ is related to the Poisson's ratio ν, $\kappa = 3-4\nu$ for plane-strain deformation and $\kappa = \frac{3-\nu}{1+\nu}$ for plane-stress deformation.

For the crack surface being traction-free, $F_x = F_y = 0$, hence $f(\xi) = 0$. Eq. (4) can then be simplified as

$$\varphi(\xi)\overline{\omega'(\xi)} + \omega(\xi)\overline{\varphi'(\xi)} + \overline{\psi(\xi)\omega'(\xi)} = 0 \tag{18}$$

Substituting Eq. (14) and (17) into Eq. (18), and recognizing $\xi\overline{\xi} = 1$ and $\overline{f(\xi)} = \overline{f}(1/\xi)$ for any point ξ on the unit circle, we have a transformed Eq. (4) in series form

$$\begin{aligned}
&2\Gamma_1 R\xi + \Gamma_1 R\sum_{n=1}^{N+2}(1-n)\overline{w_n}\xi^{n+1} + \sum_{n=1}^{N+2} p_n\xi^{1-n} + \left(\sum_{n=1}^{N+2} p_n\xi^{1-n}\right)\left(\sum_{n=1}^{N+2}(1-n)\overline{w_n}\xi^{n}\right)\\
&+\Gamma_1 R\sum_{n=1}^{N+2} w_n\xi^{1-n} + \sum_{n=1}^{N+2}(1-n)\overline{p_n}\xi^{n+1} + \left(\sum_{n=1}^{N+2} w_n\xi^{1-n}\right)\left(\sum_{n=1}^{N+2}(1-n)\overline{p_n}\xi^{n}\right)\\
&+\overline{\Gamma_2}R\xi^{-1} + \overline{\Gamma_2}R\sum_{n=1}^{N+2}(1-n)\overline{w_n}\xi^{n+1} + \sum_{n=1}^{N+2}\overline{q_n}\xi^{1-n} + \left(\sum_{n=1}^{N+2}(1-n)\overline{w_n}\xi^{n}\right)\left(\sum_{n=1}^{N+2}\overline{q_n}\xi^{1-n}\right)\\
&=0
\end{aligned} \tag{19}$$

By expanding Eq. (18) and calculating its Cauchy integral on the unit circle, we yield

$$\begin{aligned}
&\sum_{n=1}^{N+1} p_{1+n}\zeta^{-n} + \sum_{n=1}^{N}\sum_{k=1}^{N+1-n}(1-k)p_{n+k+1}\overline{w_k}\zeta^{-n} + \Gamma_1 R\sum_{n=1}^{N+1} w_{n+1}\zeta^{-n}\\
&+\sum_{n=1}^{N}\sum_{k=1}^{N+1-n}(1-k)w_{n+k+1}\overline{p_k}\zeta^{-n} + \overline{\Gamma_2}R\zeta^{-1} = 0
\end{aligned} \tag{20}$$

The above equation holds for any point ζ outside of the unit circle. Hence the coefficients of each term should vanish, from which we obtain

$$p_n + \sum_{k=1}^{N+2-n}(1-k)\overline{w_k}p_{n+k} + \sum_{k=1}^{N+2-n}(1-k)w_{n+k}\overline{p_k} + \Gamma_1 R w_n = \begin{cases}\overline{\Gamma_2}R; & n=2\\ 0; & n\neq 2\end{cases} \tag{21}$$

The unknown parameters $\varphi(\zeta)$ can then be obtained by solving Eq. (21). The SIFs at the tip of the kth branch are given as (Andersson, 1969)

$$K = K_{\mathrm{I}} - iK_{\mathrm{II}} = \frac{2\sqrt{\pi}\varphi'(\zeta_k)}{\sqrt{\omega''(\zeta_k)e^{i\delta_k}}} \tag{22}$$

where $\delta_k = \sum_{j=1}^{k-1}\theta_j$.

Specially, for a symmetrical two-branch crack, we have $M = 2$, and it represents a straight crack of length $2l$. Eq. (5) can then be written in a straightforward form

$$\omega(\zeta) = \frac{l}{2}\left(\zeta + \frac{1}{\zeta}\right) \tag{23}$$

which itself is in Laurent series. The theoretical solution of Eq. (4) is

$$\varphi(\zeta) = \frac{l}{2}\Gamma_1\zeta - \frac{l}{2\zeta}(\Gamma_1 + \overline{\Gamma_2}) \tag{24}$$

The SIFs are in the form of

$$K = \sqrt{\pi l}(2\Gamma_1 + \overline{\Gamma_2}), \tag{25}$$

which are the same as the series solutions given by Williams (1957).

The detailed procedure for calculating the SIFs of an arbitrary branched crack is given in Appendix C.

3. The stress intensity factors of a three-branched crack

When a crack is subjected to dynamic loading or running into non-uniform fields, it may split in two branches. Such crack forking or crack-branching has been broadly observed (Sundaram and Tippur, 2016; Fayyad and Lees, 2017; Dönmez and Bažant, 2020; Li et al., 2022), as shown in Fig. 2a. Here we analyze three-branched cracks as examples (when the number of crack branches M is odd) to examine the theoretical framework introduced in Section 2.

We consider a three-branched crack shown in Fig. 2b, whose free ends are labeled as z_1, z_2 and z_3, and their joint ends are denoted as h_1, h_2 and h_3, respectively. The corresponding counterparts on the unit circle are ζ_1, ζ_2, ζ_3, η_1, η_2, η_3, in turn (see Fig. 2c). The lengths of the three branches are l_1, l_2 and l_3, respectively. The angles between the two branches and the negative direction of x-axis are θ_1 and θ_2, respectively. With Eq. (5), we have the mapping function of the forked crack

$$\omega(\zeta) = \frac{R}{\zeta}(\zeta-\eta_1)^{\lambda_1}(\zeta-\eta_2)^{\lambda_2}(\zeta-\eta_3)^{\lambda_3} \tag{26}$$

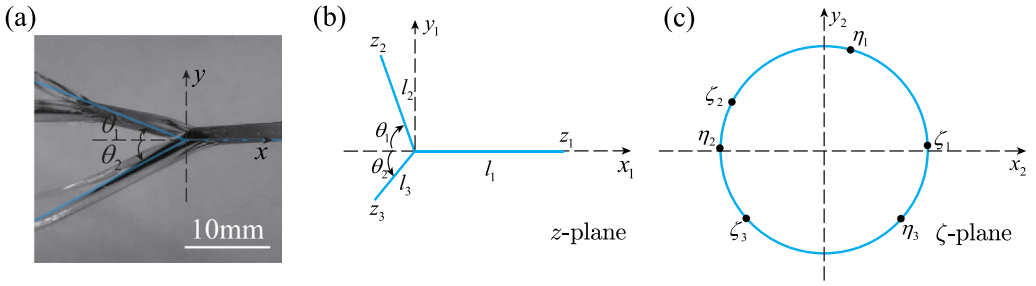

Fig. 2. Mapping of a forked crack. (a) Crack branching observed in a dynamic experiment (Sundaram and Tippur, 2018). (b) The original crack segment is horizontal and lays along the x_1-axis. The free ends of the crack are denoted as z_1, z_2 and z_3, and their respective joint points are h_1, h_2 and h_3. (c) The conformal mapping of a three-branched (forked) crack. The corresponding points on the unit circle are ζ_1, ζ_2, ζ_3, η_1, η_2, η_3, in turn.

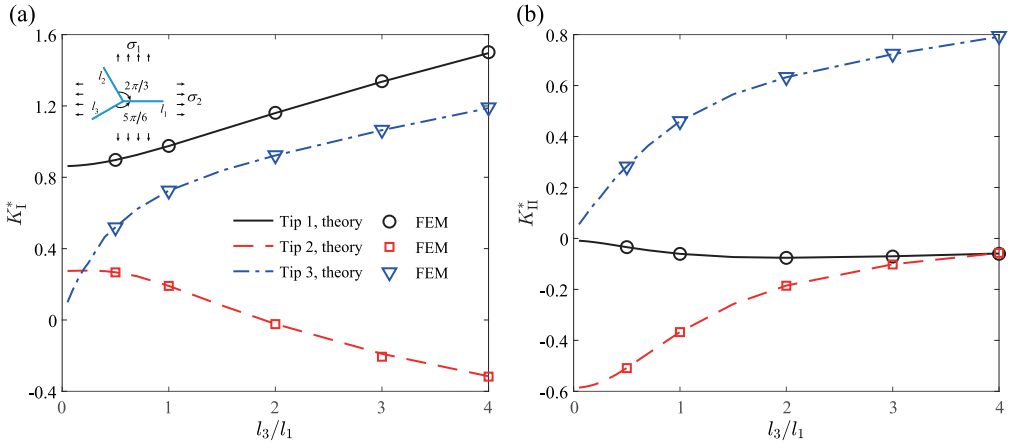

Fig. 3. A comparison of the normalized SIFs at the three tips of a forked crack between this work (lines) and FE simulations (symbols). (a)–(b), K_{I}^*, K_{II}^* as a function of l_3/l_1, respectively. Note the inset in (a) shows the boundary condition imposed to the forked crack.

where $\lambda_1 = \frac{\pi-\theta_1}{\pi}$, $\lambda_1 = \frac{\theta_1+\theta_2}{\pi}$, $\lambda_1 = \frac{\pi-\theta_2}{\pi}$. The coefficients in the Laurent expansion of the mapping function in Eq. (12) are given as

$$\begin{cases} \alpha_1 = -(\eta_1+\eta_2+\eta_3) \\ \alpha_2 = \eta_1\eta_2+\eta_1\eta_3+\eta_2\eta_3 \\ \alpha_3 = -\eta_1\eta_2\eta_3 \\ \beta_1 = -(\zeta_1+\zeta_2+\zeta_3) \\ \beta_2 = \zeta_1\zeta_2+\zeta_1\zeta_3+\zeta_2\zeta_3 \\ \beta_3 = -\zeta_1\zeta_2\zeta_3 \end{cases} \tag{27}$$

For the special case when $l_1 = l_2 = l_3 = l$ and $\theta_1 = \theta_2 = \theta$, Eq. (26) is simplified as

$$\omega(\zeta) = \frac{l}{\sqrt[3]{4}}\frac{(\zeta^3+1)^{\frac{2}{3}}}{\zeta} = \frac{l}{\sqrt[3]{4}}\left(\zeta^{\frac{3}{2}}+\frac{1}{\zeta^{\frac{3}{2}}}\right)^{\frac{2}{3}} \tag{28}$$

3.1. Finite-element verification

we adopt FEM to verify this theoretical framework for the forked crack shown in Fig. 2b. We consider a sufficiently large sample by setting both side of the sample to be $20l$. The length of each part of the crack is $l_1 = l$, $l_2 = l$, and l_3 is variable. The angles of the two branches with respect to the x-axis are $2\pi/3$ and $5\pi/6$, respectively. Stress singularity at the crack tip is captured by using collapsed elements with duplicate nodes in the shape of sweeping quadrilateral. Normalized SIFs $K_{\mathrm{I}}^* = K_{\mathrm{I}}/\sqrt{\pi\sigma(l_1+l_2)/2}$ and $K_{\mathrm{II}}^* = K_{\mathrm{II}}/\sqrt{\pi\sigma(l_1+l_2)/2}$ as functions of the normalized length of the third branch l_3/l_1, is shown in Fig. 3a–b. The lines are based on theoretical predictions and the symbols correspond data from FE simulations. The theoretical predictions match well with those from FE simulation.

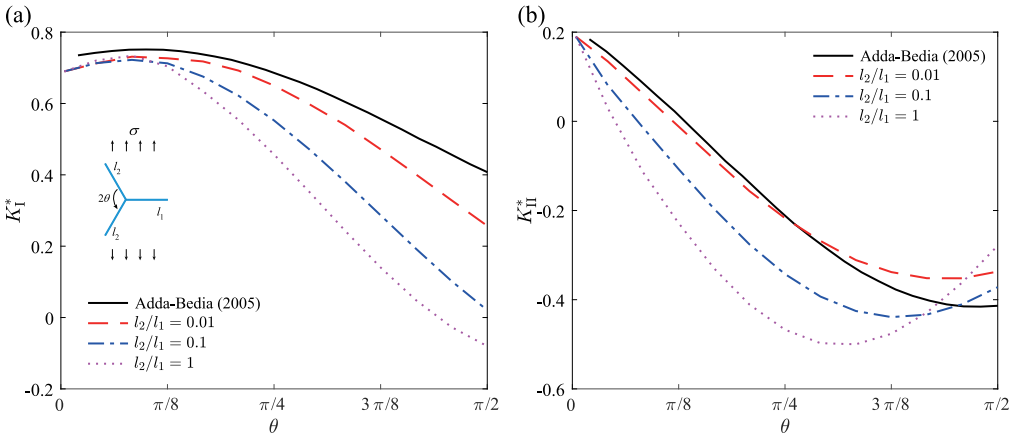

Fig. 4. A comparison of the normalized SIFs at Tip 2 between this work and the work by Adda-Bedia (2005). Here we consider a large sample with a symmetrically branched crack subject to uniaxial loading perpendicular to the primary part of the crack.

3.2. Symmetrical three-branched cracks

We start with a three-branched crack with symmetrical branches, which means two branches of the crack are equal, i.e. $l_2 = l_3$, and $\theta_1 = \theta_2 = \theta$. By using Eq. (22) we obtain the SIFs of the three-branched crack. In order to analyze possible crack propagation of the branched cracks, we calculate the energy release rate at all tips of all the three branches, by adopting the following equation between G and K (Hussain et al., 1973; Zeng and Wei, 2017)

$$G = \begin{cases} \dfrac{K_I^2 + K_{II}^2}{E^*}; & K_I \le 0 \\ \dfrac{K_{II}^2}{E^*}; & K_I < 0 \end{cases} \tag{29}$$

where E^* is the modified Young's modulus of the material, $E^* = E$ for plane-stress deformation and $E^* = \frac{E}{1-\nu^2}$ for plane-strain deformation. When $K_I < 0$, it implies the scenario of relative penetration between the upper and the lower surfaces of the crack, and the mode-I fracture does not contribute to the energy leading to the propagation of crack. Therefore, we set $K_I = 0$ in this circumstance to ensure the accuracy of G. In linear elastic fracture, the energy release rate G is equivalent to the J-integral (Rice, 1968), and those tips with greater J-integral will precede to other tips to propagate. We normalize K_I, K_{II} and G as $K_I^* = K_I/\sqrt{\pi\sigma(l_1+l_2)/2}$, $K_{II}^* = K_{II}/\sqrt{\pi\sigma(l_1+l_2)/2}$ and $G^* = GE^*/[\sigma^2\pi(l_1+l_2)/2]$, respectively, to demonstrate the relations among SIFs, energy release rate and geometrical parameters.

Adda-Bedia (2005) employed the conformal mapping to solve the SIFs of a three-branched crack with symmetrical branches. Here we supply a comparison between this work and Adda-Bedia (2005) shown in Fig. 4. A three-branched crack with two symmetrical branches is subjected to a uniaxial loading (see the inset), and K_I^*, K_{II}^* are functions of θ. As Adda-Bedia made the approximation that $l_2/l_1 \ll 1$ to simplify the mapping function, his results match well with ours when l_2/l_1 is considerably small ($l_2/l_1 < 0.01$, as shown in Fig. 4). Nevertheless, significant differentials exist when l_2/l_1 becomes large.

In Fig. 5a, we show a symmetrical three-branched crack, of which $\theta_1 = \theta_2 = \pi/3$ and $l_1 = l_2 = l_3 = l$ (see the inset). This crack is subjected to biaxial loading, with σ_1 in the longitudinal direction and σ_2 in the transversal direction. Let the sum of σ_1 and σ_2 be fixed, i.e. $\sigma_1 + \sigma_2 = \sigma$. Due to the symmetry of this BVP, K_I and G of tip 2 and tip 3 are equal, and K_{II} of tip 2 and tip 3 are of opposite sign. We show in Fig. 5 the log-plot of K_I^*, K_{II}^* and G^* versus σ_2/σ_1. From Fig. 5c, when $\sigma_1 > \sigma_2$, tip 1 will propagate first; if $\sigma_1 < \sigma_2$, tip 2 and tip 3 will be the first to propagate.

We further explore the influence of geometrical parameters to the SIFs of symmetrical three-branched cracks subjected to uniaxial loading. The two parameters determining the shape of a symmetrical three-branched crack are θ and l_2/l_1. In Fig. 6, we show the relations between K_I^*, K_{II}^*, G^* and the two variables θ and l_2/l_1. The main crack (tip 1) is Mode I dominant as θ and l_2/l_1 change. From Fig. 6c and f, it is evident that the main crack is likely to propagate first when such a symmetrical three-branched crack is subjected to longitudinal loading.

3.3. T-shaped cracks

Another type of three-branched cracks of particular engineering significance is the T-shaped cracks. We consider the special case in which the branched crack is perpendicular to the main crack, i.e. $\theta_1 = \theta_2 = \pi/2$. For the convenience of discussion, we normalize K_1, K_2 and G by letting $K_I^* = K_I/\sqrt{\pi\sigma l_1/2}$, $K_{II}^* = K_{II}/\sqrt{\pi\sigma l_1/2}$ and $G^* = GE^*/(\sigma^2\pi l_1/2)$, respectively.

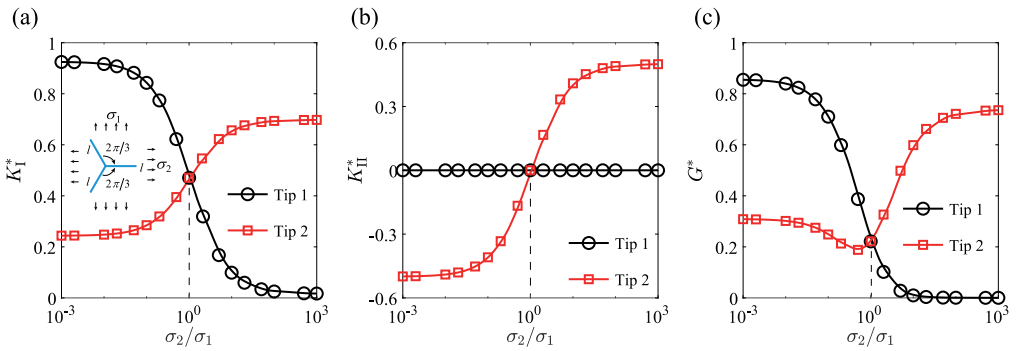

Fig. 5. A three-branched crack with symmetrical branches subjected to biaxial loading. (a)–(c) K_I^*, K_{II}^*, G^* as a function of σ_2/σ_1, respectively. Note the inset in (a) shows the boundary condition imposed to the forked crack.

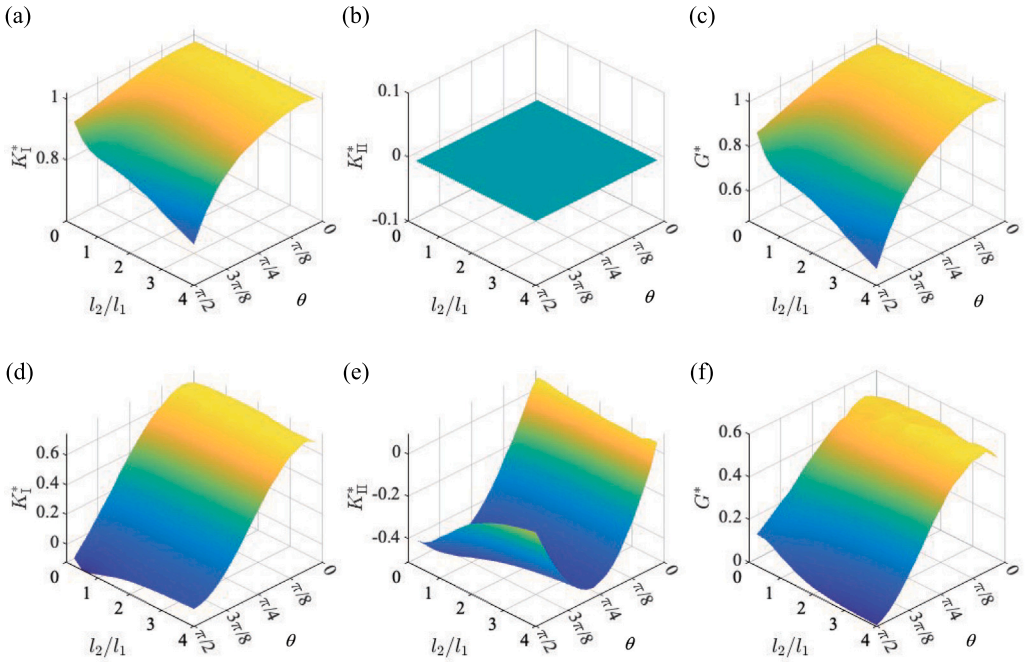

Fig. 6. Three-dimensional diagrams to show the normalized SIFs K_I^* and K_{II}^* and energy release rate G^* as a function of both θ and l_2/l_1. (a)–(c)K_I^*, K_{II}^* and G^* at tip 1 and (d)–(f) the three parameters at tip 2.

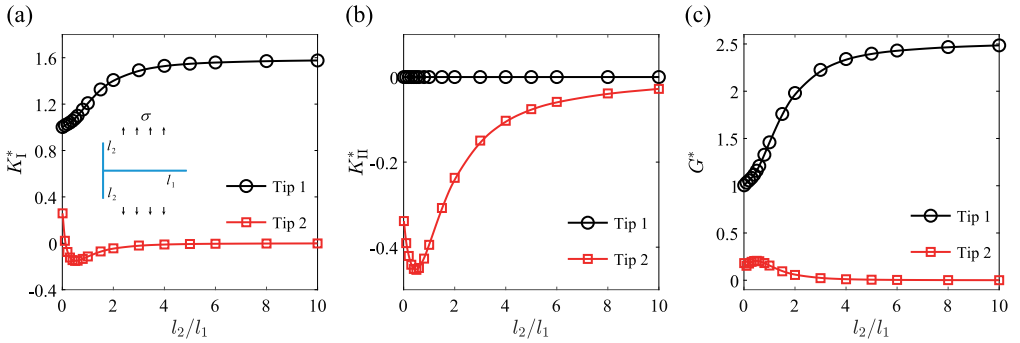

Fig. 7. A symmetrical T-shaped (three-branched) crack subjected to uniaxial loading, where $l_2 = l_3$. (a)–(c) are normalized SIFs K_I^* and K_{II}^* and energy release rate G^* as a function of l_2/l_1, respectively. Note the inset in (a) shows the boundary condition imposed to the T-shaped crack.

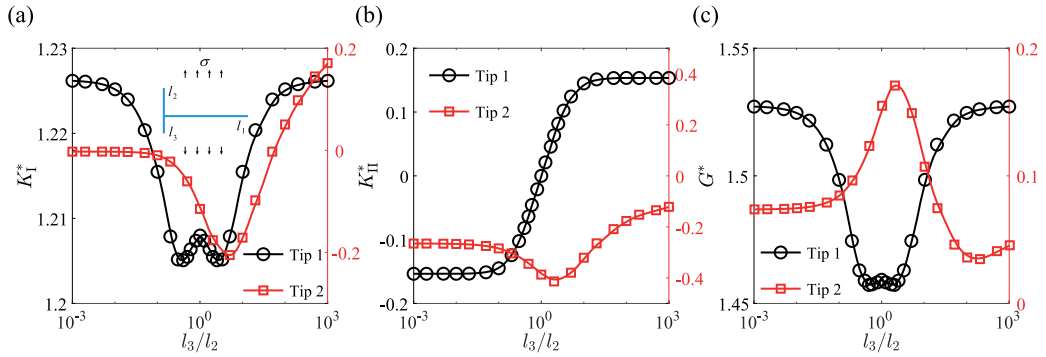

Fig. 8. A T-shaped three-branched crack subjected to uniaxial loading. (a)–(c) normalized SIFs K_I^* and K_{II}^* and energy release rate G^* as a function of the ratio of two branches l_3/l_2, respectively. Note the inset in (a) shows the boundary condition imposed to the T-shaped crack.

Considering the simple case that we have two equal vertical branches, i.e. $l_2 = l_3$, we show in Fig. 7 K_I^*, K_{II}^* and G^* as a function of l_2/l_1. The symmetry of the BVP gives rise to identical K_I and G at tip 2 and tip 3, while K_{II} of the two tips are of opposite sign. When l_2/l_1 approaches to 0, we see from Fig. 7a and b that K_I^* and K_{II}^* of the main crack (tip 1) approach to 1 and 0, respectively. The results are in consonance with the theoretical solution of a straight crack. K_I^* of the main crack increases as l_2/l_1 increases, and it eventually converges to ~ 1.6. In contrast, K_I^* and K_{II}^* approach to 0 as l_2/l_1 increases. The result in Fig. 7c implies that the main crack is always the first to propagate in this BVP.

We now examine the influence of the ratio of the two vertical branches l_3/l_2. We consider a T-shaped crack shown in Fig. 8a and the crack is subjected to uniaxial loading. For the convenience of discussion, we let $l_2 + l_3 = l = 2l_1$. In Fig. 8, we plot K_I^*, K_{II}^* and G^* as the functions of l_3/l_2. When $l_3/l_2 \neq 1$, mode II fracture at the tip of the main crack, due to the asymmetry of the branched crack, will dominate late on crack propagation, as seen from Fig. 8b. Such a conclusion is further confirmed by looking at the energy release rate shown in Fig. 8c, where crack propagation in the main crack is preferred over the vertical ones for the specific boundary condition (see the insert in Fig. 8a).

4. The stress intensity factors of a four-branch crack

We now apply the solution established in Section 2 to cracks of four branches. Such type of cracks are also rather common in engineering practice, and have been broadly observed in experiments (Xu et al., 2003; Burghard et al., 2004), as demonstrated in Fig. 9a-b. The four-branched cracks serve as examples when the number of crack branches M is even.

We consider an arbitrarily sized four-branched crack shown in Fig. 9c. The ends of this branched crack are labeled as z_1, z_2, z_3 and z_4, and the joint points in turn are h_1, h_2, h_3 and h_4. The length of the branches are l_1, l_2, l_3 and l_4, respectively. The corresponding counterparts on the mapped unit circle are ζ_1, ζ_2, ζ_3, ζ_4, η_1, η_2, η_3 and η_4, in sequence, as shown in Fig. 9d. With Eq. (5), we obtain the mapping function as

$$\omega(\zeta) = \frac{R}{\zeta}(\zeta-\eta_1)^{\lambda_1}(\zeta-\eta_2)^{\lambda_2}(\zeta-\eta_3)^{\lambda_3}(\zeta-\eta_4)^{\lambda_4} \tag{30}$$

where $\lambda_n = \frac{\theta_n}{\pi}$. When expanding the mapping function in Eq. (30) in Laurent series, we obtain equations for those the coefficients in terms of points on the unit circle in the ζ-plane (seen in Eq. (12))

$$\begin{cases} \alpha_1 = -(\eta_1+\eta_2+\eta_3+\eta_4) \\ \alpha_2 = \eta_1\eta_2+\eta_1\eta_3+\eta_1\eta_4+\eta_2\eta_3+\eta_2\eta_4+\eta_3\eta_4 \\ \alpha_3 = -(\eta_1\eta_2\eta_3+\eta_2\eta_3\eta_4+\eta_1\eta_3\eta_4+\eta_1\eta_2\eta_4) \\ \alpha_4 = \eta_1\eta_2\eta_3\eta_4 \\ \beta_1 = -(\zeta_1+\zeta_2+\zeta_3+\zeta_4) \\ \beta_2 = \zeta_1\zeta_2+\zeta_1\zeta_3+\zeta_1\zeta_4+\zeta_2\zeta_3+\zeta_2\zeta_4+\zeta_3\zeta_4 \\ \beta_3 = -(\zeta_1\zeta_2\zeta_3+\zeta_2\zeta_3\zeta_4+\zeta_1\zeta_3\zeta_4+\zeta_1\zeta_2\zeta_4) \\ \beta_4 = \zeta_1\zeta_2\zeta_3\zeta_4 \end{cases} \tag{31}$$

The above equations enable us to determine the coefficients of the Laurent series of the mapping function, and from which we can derive the SIFs at all tips of the four-branched crack.

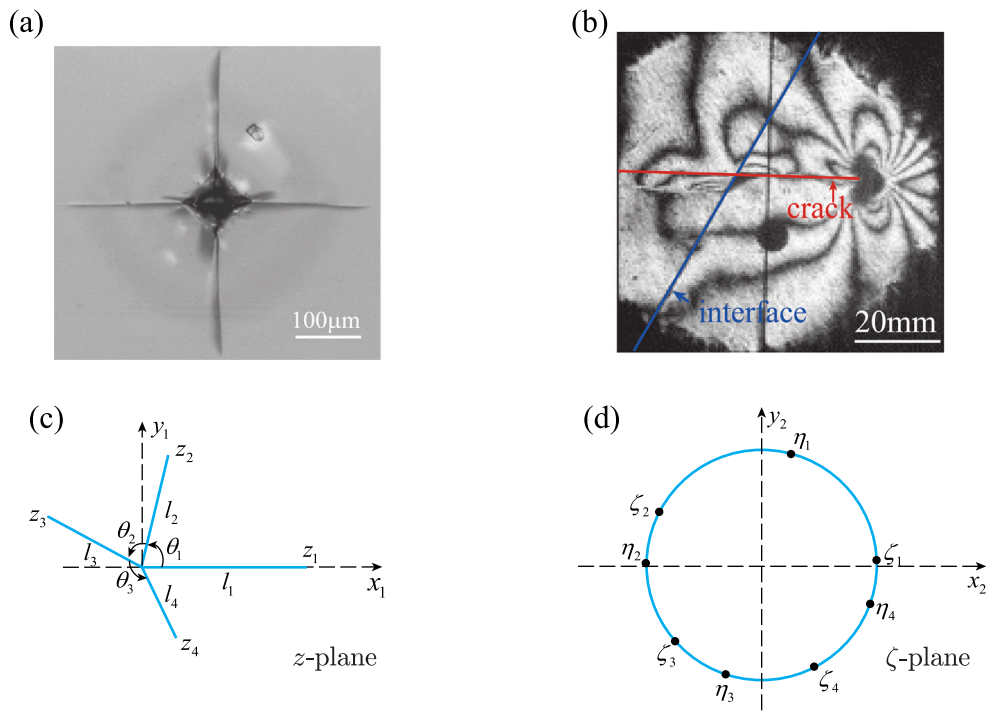

Fig. 9. Four-branched cracks observed in experiments and their conformal mapping to unit circles. (a) The four-branched crack after indentation (Burghard et al., 2004). (b) One straight crack intersecting an interface in a dynamic experiment (Xu et al., 2003). (c) The crack on the z-plane: the original part is horizontal to the x_1-axis. The ends of the crack are z_1, z_2, z_3 and z_4, and the joint points are h_1, h_2, h_3 and h_4. (d) The corresponding points on the mapped unit circle are ζ_1, ζ_2, ζ_3, ζ_4, η_1, η_2, η_3, η_4, in turn.

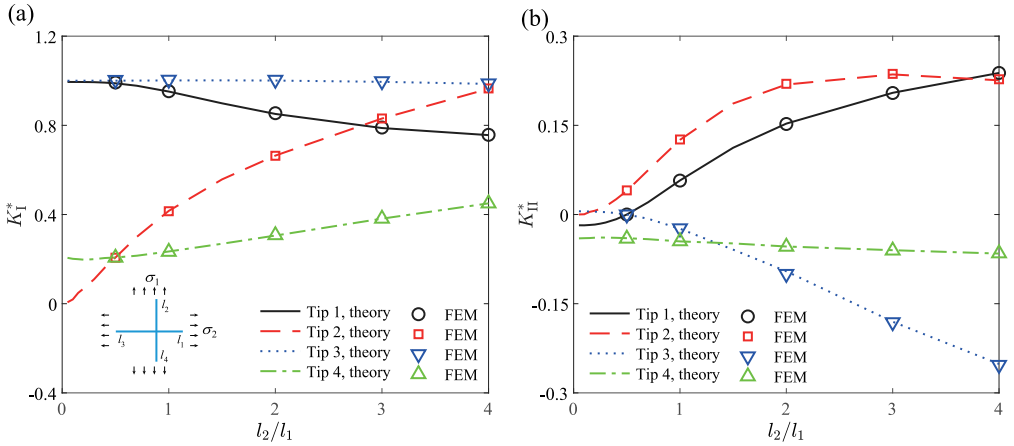

Fig. 10. A comparison of normalized SIFs at the four tips of a cruciform crack, where $l_3/l_1 = 4$ and $l_4/l_1 = 0.5$, this work (lines) vs. FE simulations (symbols). (a) and (b) K_I^*, K_{II}^* as a function of l_2/l_1, respectively. Note the inset in (a) shows the boundary condition imposed to the cruciform crack.

4.1. Finite-element verification

We adopted the FE model shown in Fig. 10a to verify the theoretical framework. We consider a sufficient large sample by setting both side of the sample to be $20l$. For simplicity, we consider a crack with the following branch length, $l_1 = l$, $l_3 = 4l$, $l_4 = 0.5l$ and l_2 being a variable. The angles between each branch are $\theta_1 = \theta_2 = \theta_3 = \pi/2$. The cracked body is subjected to a biaxial loading with $\sigma_1 = \sigma_2 = \sigma$. Stress singularity at the crack tips is captured by using collapsed elements with duplicate nodes in the shape of sweeping quadrilateral. Normalized SIFs $K_I^* = K_I/\sqrt{\pi\sigma(l_1+l_3)/2}$ and $K_{II}^* = K_{II}/\sqrt{\pi\sigma(l_1+l_3)/2}$ as a function of l_2/l_1 are shown in Fig. 10. Here the lines represent predictions by using this theory and the symbols are data from FE simulations. The results from our theory agree well with those from FE simulations.

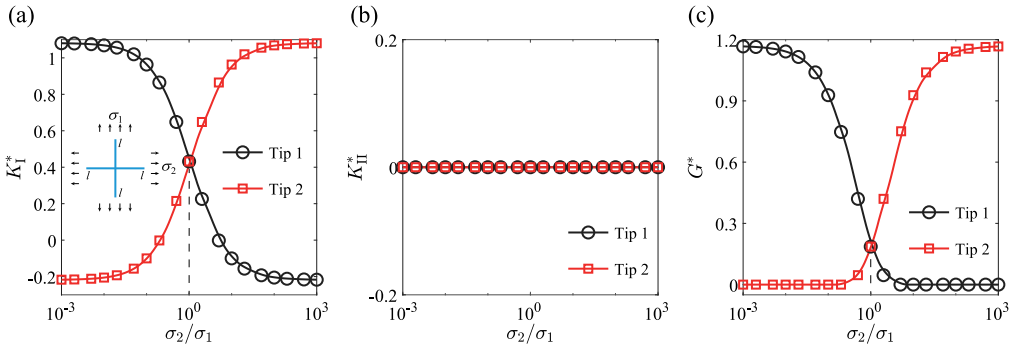

Fig. 11. A symmetrical cruciform crack, where $l_1 = l_2 = l_3 = l_4 = l$, subjected to biaxial loading. (a)–(c) K_I^*, K_{II}^*, G^* as a function of σ_2/σ_1, respectively. Note the inset in (a) shows the boundary condition imposed to the cruciform crack.

4.2. Cruciform cracks

Now we apply the theory to cruciform cracks, which are commonly seen in indentation experiment (Burghard et al., 2004). Specifically, when $l_1 = l_2 = l_3 = l_4 = l$ and $\theta_1 = \theta_2 = \theta_3 = \pi/2$, it describes the simplest cruciform crack. The mapping function of this particular crack is in the form of

$$\omega(\zeta) = \frac{l}{\sqrt{2}} \frac{(\zeta^4 + 1)^{\frac{1}{2}}}{\zeta} = \frac{l}{\sqrt{2}} \left(\zeta^2 + \frac{1}{\zeta^2} \right)^{\frac{1}{2}} \tag{32}$$

A typical cruciform crack has two straight cracks intersecting at the right angle, i.e. $\theta_1 = \theta_2 = \theta_3 = \pi/2$. We consider the transversal crack as the main crack and the longitudinal one as two vertical branches. For convenience, we present the normalized K_I, K_I and G by defining $K_I^* = K_I/\sqrt{\pi\sigma(l_1 + l_3)/2}$, $K_{II}^* = K_{II}/\sqrt{\pi\sigma(l_1 + l_3)/2}$ and $G^* = GE^*/[\sigma^2\pi(l_1 + l_3)/2]$, respectively.

We consider the influence of loading condition on crack propagation in an infinite body with a symmetrical cruciform crack. The length of its branches is equal, i.e. $l_1 = l_2 = l_3 = l_4$. Due to the symmetry of the BVP, K_I of tip 1 and tip 3 are the same, and K_I of tip 2 is the same with tip 4. K_{II} of the pairing tips are of opposite signs. The crack is subjected to biaxial loading with longitudinal stress σ_1 and transversal stress σ_2, respectively. For discussion, we assume $\sigma_1 + \sigma_2 = \sigma$ and σ is fixed.

In Fig. 11, we show K_I^*, K_{II}^* and G^* are functions of σ_2/σ_1. From Fig. 11c, when $\sigma_1 > \sigma_2$, the main crack (tip 1 and tip 3) is the first to propagate, and when $\sigma_1 < \sigma_2$, the vertical branches (tip 2 and tip 4) start to propagate first.

Now we turn to the influence of the length of the vertical branches, and assume the length of the two vertical branches are equal, i.e. $l_2 = l_4$. The sample is subjected to a uniaxial loading, as illustrated in the inset of Fig. 12a. Figs. 12a to c show in turn K_I^*, K_{II}^* and G^* as a functions l_2/l_1. We see from Fig. 12a that K_I^* of the main crack (tip 1 and tip 3) converges to 1 when l_2/l_1 approaches 0 if $\sigma_2 = 0$, and it converges to 0 when $\sigma_1 = 0$. These results are in consistent with the theoretical solutions of a straight crack in corresponding loading conditions. Under longitudinal loading, K_I^* converges to about 1.12 when l_2/l_1 is about 4 or greater. When the cruciform crack is subjected to uniaxial loading, the branches perpendicular to the loading direction have the potential to propagate. The branches parallel to the loading direction tend to close, on the contrary.

We also explore the influence of the ratio of two vertical branches on the propagation of the main crack (tip 1 and tip 3) when the sample is subjected to a uniaxial loading. For convenience, we keep $l_2 + l_3 = l = 2l_1$. We show in Fig. 13 K_I^*, K_{II}^* and G^* as functions of l_3/l_2. When the lengths of the two vertical parts are not equal, i.e. $l_2 \neq l_3$, the asymmetry nature of the branched crack leads to Mode II fracture at the tip of the main crack, as shown in Fig. 13b. We see from Fig. 13c that the main crack is always the first to propagate.

4.3. Two intersecting straight crack

If we take a step back from the cruciform cracks and consider a branched crack formed by the intersection of two straight cracks (or interfaces), we have a four-branched crack commonly seen in engineering practice, like similar crack patterns formed during hydraulic fracking. An example of such cracks for experimental exploration (Xu et al., 2003) is shown in Fig. 9b. For this kind of four-branched crack, we have $\theta_1 = \theta_3 = \theta$ and $\theta_2 = \pi - \theta$. For demonstration, we explore the scenario when the four branches of the crack are equal, i.e. $l_1 = l_2 = l_3 = l_4 = l$. For this instance and when θ approaches 0, both K_I^* and G^* of tip 1 and tip 2 are the same, and K_{II}^* of those two tips are of opposite sign, as given in Fig. 14. From Fig. 14c, we find that the crack prefers to propagate from tip 1 and tip 3 over the other two branch tips given the much greater energy release rate at tip 1 and tip 3.

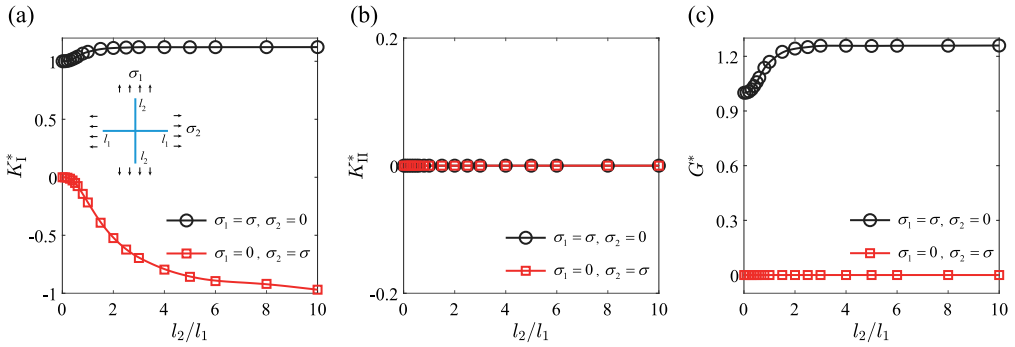

Fig. 12. A cruciform crack subjected to biaxial loading, respectively. (a)–(c) K_I^*, K_{II}^*, G^* as a function of l_2/l_1, respectively. Note the inset in (a) shows the boundary condition imposed to the cruciform crack.

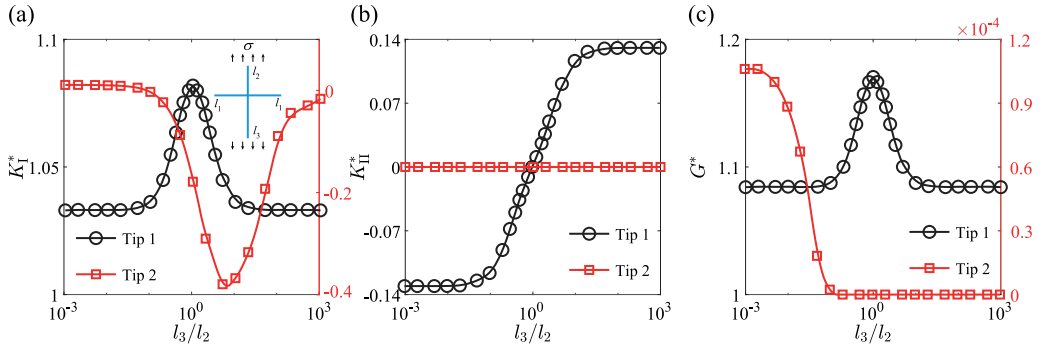

Fig. 13. A cruciform crack subjected to uniaxial loading. (a)–(c) K_I^*, K_{II}^*, G^* as a function of l_3/l_2, respectively. Note the inset in (a) shows the boundary condition imposed to the cruciform crack.

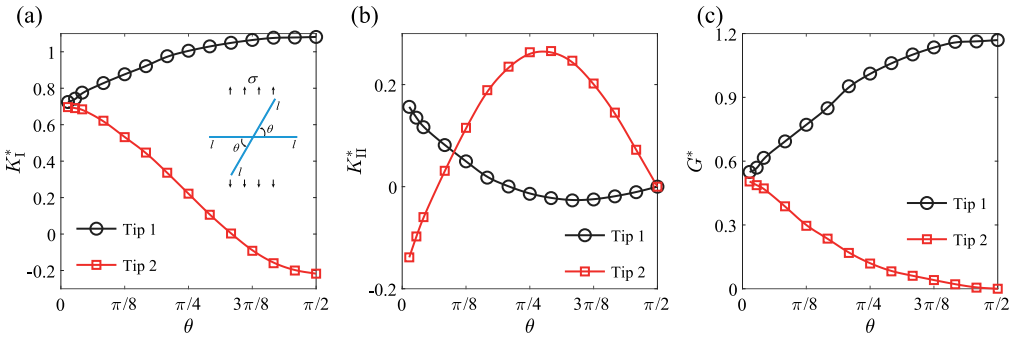

Fig. 14. A four-branched crack subjected to uniaxial loading. (a)–(c) K_I^*, K_{II}^*, G^* as a function of θ, respectively. Note the inset in (a) shows the boundary condition imposed to the four-branched crack.

5. Conclusions

Crack branching is of great significance in engineering practice and is a highly complex process. One of the core issue associated with the widely used energy based criterion is to find the SIFs of the crack. In this work we establish a theoretical framework to calculate the SIFs of an arbitrary branched crack in a infinite space. By using Schwarz–Christoffel mapping, we transform the branched crack on the z-plane into a unit circle on the ζ-plane to simplify the BVP. We solve the BVP and obtain the complex analytical functions, from which we further deduced the SIFs at all crack branches. This theoretical framework were applied to analyze SIFs of three-branched and four-branched cracks, which are commonly seen in engineering practice. The accuracy of the theoretical results were also validated through FE simulations. It should be emphasized we choose the geometries of those three and four-branched cracks in a random manner. It by no means suggests that the theory is only applicable to those examples. It should work for most branched cracks. We expect the theoretical method we established here can serve as a theoretical tool to calculate the SIFs of any arbitrary branched crack. An apparent direction worth further exploration is to extend the theory for crack branching in

a half space or even in finite domains, which could then be more practical from engineering perspective. The theoretical approach to calculate SIFs of branched crack can help to understand crack branching and crack deflecting. With known SIFs of branched cracks and adopting the crack-path selection criterion, we may foresee the path of crack extension and therefore the formation of crack patterns. It has also been suggested that even SIFs of branched cracks in quasi-static condition could be meaningful to understand crack branching during dynamic fracture (Adda-Bedia, 2005). Success in those problems may eventually help to predict where a branched crack propagates and how to form a complex crack network, which may be desired either for safety analysis or for crack engineering.

CRediT authorship contribution statement

Zhuo-Er Liu: Formal analysis, Investigation, Validation, Visualization, Writing – original draft, Writing – review & editing. **Yujie Wei:** Formal analysis, Methodology, Supervision, Funding acquisition, Writing – original draft, Writing – review & editing.

Declaration of competing interest

The authors declare that they have no known competing financial interests or personal relationships that could have appeared to influence the work reported in this paper.

Data availability

Data will be made available on request.

Acknowledgments

The authors acknowledge supports from the NSFC Basic Science Center for 'Multiscale Problems in Nonlinear Mechanics' (No. 11988102).

Appendix A. Discontinuities on the path of the singular integral equation

In Section 2 we mention that the multi-value nature of mapping function and the possible discontinuities make it rather difficult to employ Schwarz–Christoffel mapping to solve the BVPs directly. Here we will discuss the influence of these discontinuities on solving the BVPs.

The BVPs of a branched crack can be reduced to singular integral equation by employing the Cauchy integral form of Eq. (4) on the path of the unit circle C as

$$\int_C \frac{\varphi(\xi)}{\xi-\zeta}d\xi + \int_C \frac{\omega(\xi)}{\overline{\omega'(\xi)}}\frac{\overline{\varphi(\xi)}}{\xi-\zeta}d\xi + \int_C \frac{\overline{\psi(\xi)}}{\xi-\zeta}d\xi = \int_C \frac{f(\xi)}{\xi-\zeta}d\xi \tag{A.1}$$

For $\frac{\omega(\xi)}{\overline{\omega'(\xi)}}$ in the second term of Eq. (A.1), there is

$$\frac{\omega(\xi)}{\overline{\omega'(\xi)}} = \frac{\omega(\xi)}{\overline{\omega(\xi)}}\frac{\overline{\omega(\xi)}}{\overline{\omega'(\xi)}} = \frac{\omega(\xi)}{\overline{\omega(\xi)}}\frac{\prod_{n=1}^{M}(1-\overline{\eta}_n\xi)}{\xi\prod_{n=1}^{M}(1-\overline{\zeta}_n\xi)} \tag{A.2}$$

where

$$\frac{\omega(\xi)}{\overline{\omega'(\xi)}} = \begin{cases} 1; & \xi \in \widehat{\eta_M\eta_1} \\ e^{2i\theta_1}; & \xi \in \widehat{\eta_1\eta_2} \\ \vdots & \\ e^{2i\sum_{n=1}^{M-1}\theta_n}; & \xi \in \widehat{\eta_{M-1}\eta_M} \end{cases} \tag{A.3}$$

Therefore, $\zeta_1, \zeta_2, \ldots, \zeta_M$ are M poles for Eq. (A.1), and $\eta_1, \eta_2, \ldots, \eta_M$ are M jump discontinuities for Eq. (A.1), respectively.

To avoid the influence of these discontinuities, we make some transformation and approximation to the BVPs. First, Eq. (4) is reformulated into Eq. (18) and the M poles on the unit circle C are eliminated. We also adopt polynomial approximation to smooth the image of mapping function near $\omega(\eta_k)$ to avoid the jump discontinuities. As shown in Fig. A.1, the image of the approximate mapping function approaches to the original crack as the terms of Laurent series N increasing.

Liu and Wei (2021) gave an analytical solution of both the SIFs and the stress fields of kinked cracks. However, the results of SIFs deviate from the FE simulation when the kink length l is much smaller than the main crack a ($l/a < 0.2$). The reason is the authors neglect the discontinuities on the path of the singular integral equation (Eq. (A.1)) when solving the BVPs. In the kinking problem, the corresponding points of the crack tips and the joint point of the crack in the ζ-plane are ζ_1, ζ_2, η_1 and η_2, respectively, and they are also the discontinuities on the path of the Eq. (A.1). When kink length approaches to 0, η_1 and η_2 will approach to ζ_1, and these two jump discontinuities will influence the accuracy of the solutions of Eq. (A.1) near the crack tip.

In this work we have overcome this drawback by making the approximation of the mapping functions as present in Section 2. Here we compare the SIFs of a kinked crack by using different theoretical methods including Cotterell and Rice (1980), He et al. (1991), Liu and Wei (2021) and this work. The kinked crack is subjected to uniaxial loading (see the inset), and the normalized SIFs are given as functions of l/a, as shown in Fig. A.1(d)–(e). The SIFs given by this work match well with the FE results for arbitrary l/a. The analytical solution given by Liu and Wei (2021) is still applicable in practice when $l/a > 0.2$.

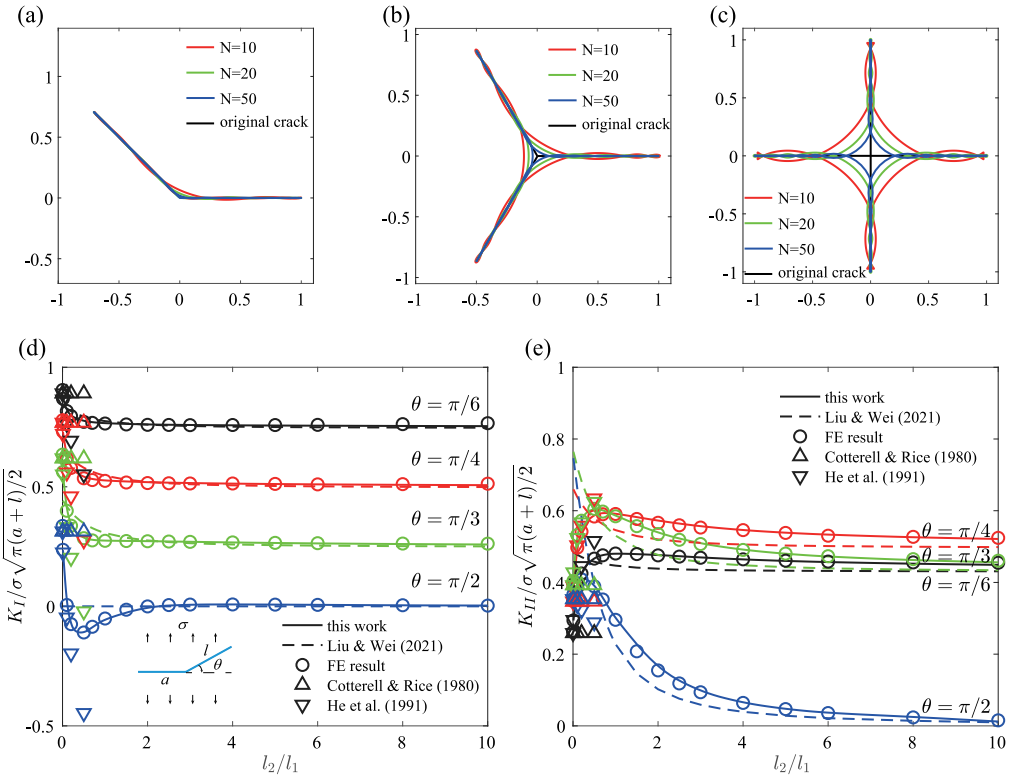

Fig. A.1. Image of the mapping function in different terms of Laurent series. (a) kinked crack, (b) three-branched crack and (c) four-branched crack. (d)–(f) is the comparison of the SIFs of a kinked crack among this work, Liu and Wei (2021),Cotterell and Rice (1980), He et al. (1991) and the FE results.

Appendix B. First order derivative of the mapping function $\omega(\zeta)$

Here we give a method to deduce the first order derivative of the mapping function $\omega(\zeta)$ in Eq. (9). The definition of the SIFs at the kth tip of a M-branched crack is in the form of

$$K = 2\sqrt{2\pi}\lim_{z\to z_k}\sqrt{z-z_k}\varphi'(z) = 2\sqrt{2\pi}\lim_{\zeta\to\zeta_k}\sqrt{\omega(\zeta)-\omega(\zeta_k)}\frac{\varphi'(\zeta)}{\omega'(\zeta)} \tag{B.1}$$

where z_k is the coordinate of the kth tip in the z-plane and ζ_k is its counterpart in the ζ-plane. This limitation exists when $\lim_{\zeta\to\zeta_k}\omega'(\zeta) = 0$. Therefore, $\zeta_1, \ldots, \zeta_M$ are the M zeros of $\omega'(\zeta)$.

The first order derivative of $\omega(\zeta)$ in Eq. (5) is

$$\begin{aligned}\omega'(\zeta) &= -\frac{R}{\zeta^2}\prod_{n=1}^{M}(\zeta-\eta_n)^{\lambda_n} + \frac{R}{\zeta}\sum_{n=1}^{M}\frac{\lambda_n\prod_{k=1}^{M}(\zeta-\eta_k)^{\lambda_k}}{\zeta-\eta_n}\\ &= \frac{R}{\zeta}\prod_{n=1}^{M}(\zeta-\eta_n)^{\lambda_n}\left(-\frac{1}{\zeta}+\sum_{n=1}^{M}\frac{\lambda_n}{\zeta-\eta_n}\right)\\ &= \omega(\zeta)\frac{\sum_{n=0}^{M}A_n\zeta^{M-n}}{\zeta\prod_{n=1}^{M}(\zeta-\eta_n)}\\ &= \omega(\zeta)\frac{H(\zeta)}{\zeta\prod_{n=1}^{M}(\zeta-\eta_n)}\end{aligned} \tag{B.2}$$

where $H(\zeta)$ is a M-order polynomial of ζ and A_n is coefficient of the nth term. Since $\zeta_1, \ldots, \zeta_M$ are the M zeros of $\omega'(\zeta)$, they are also the M zeros of $H(\zeta)$. Therefore, $H(\zeta)$ can be written in the form of

$$H(\zeta) = A_0\prod_{n=1}^{M}(\zeta-\zeta_n) \tag{B.3}$$

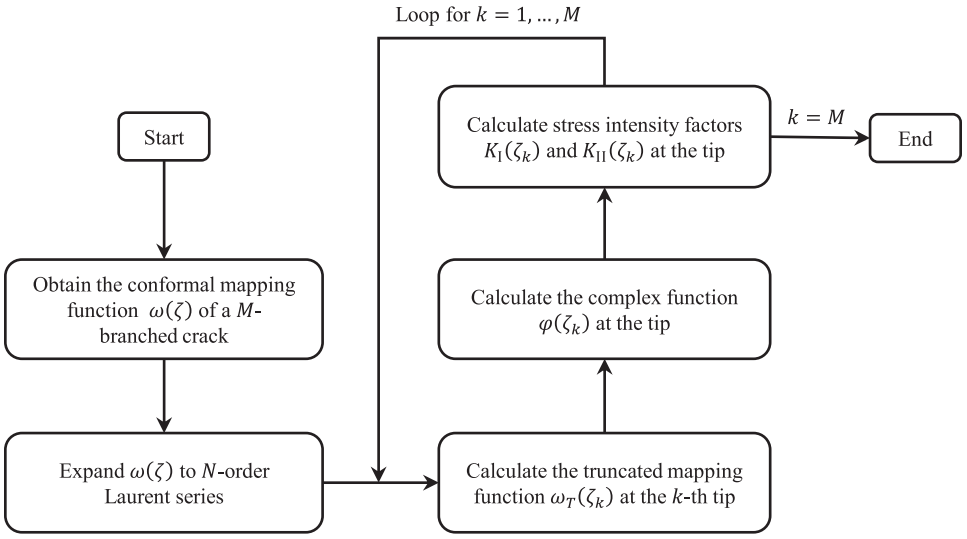

Fig. C.1. The flow chart to show detailed procedures in calculating the SIFs at the tips of a M-branched crack.

where A_0 is the coefficient of ζ^M in $H(\zeta)$. From Eq. (B.2), coefficient A_0 is in the form of

$$A_0 = -1 + \sum_{n=1}^{M} \lambda_n = -1 + \frac{1}{\pi} \sum_{n=1}^{M} \theta_n = 1 \tag{B.4}$$

By substituting Eqs. (B.3) and (B.4) into Eq. (B.2), we have

$$\omega'(\zeta) = \omega(\zeta) \frac{\prod_{n=1}^{M} (\zeta - \zeta_n)}{\zeta \prod_{n=1}^{M} (\zeta - \eta_n)} \tag{B.5}$$

which is the result shown in Eq. (9).

Appendix C. Procedure for calculating stress intensity factors

We calculate SIFs K_I and K_{II} with following procedures. The detailed procedure flow chart is shown in Fig. C.1.

First we need to obtain the conformal mapping function of the M-branched crack into a unit circle. As mentioned in Section 2, the mapping function given by Eq. (5) contains $2M+1$ real parameters $\mu_1, \ldots, \mu_M, \nu_1, \ldots, \nu_M$ and R. These parameters are determined by solving the $2M+1$ equations in Eq. (6). These nonlinear equations can be solved numerically by employing Newton–Raphson method.

Next we need to expand the mapping function $\omega(\zeta)$ in the N-order Laurent series as

$$\omega(\zeta) \approx R \left(\zeta + \sum_{n=1}^{N} a_n \zeta^{1-n} \right) \tag{C.1}$$

where the coefficients $a_1, a_2, \ldots, a_N$ are given in Eq. (13). The order N is decided by an examination that the N-order Laurent expansion of the mapping function $\omega_N(\zeta)$ satisfies $\omega'_N(\zeta) \approx \omega'(\zeta)$ and $\omega''_N(\zeta) \approx \omega''(\zeta)$, simultaneously (Bowie, 1964). In this work, our exploration shows $N = 770$ a reasonable number for most cases of branched cracks.

The following steps are based on a specific crack. Take the kth tip as an example for illustration. In order to obtain the truncated mapping function at tip k, we need to calculate the accurate first and second order derivative $\omega'(\zeta_k)$ and $\omega''(\zeta_k)$, where $\zeta_k = e^{i\mu_k}$ is the corresponding point of the kth tip on the unit circle. The additional coefficients T_1 and T_2 in the truncated mapping function $\omega_T(\zeta_k)$ are obtained by solving the two linear equations

$$\begin{cases} N\zeta_k^{-N-1} T_1 + (N+1)\zeta_k^{-N-2} T_2 = 1 + \sum_{n=1}^{N} (1-n) a_n \zeta_k^{-n} \\ N(N+1)\zeta_k^{-N-2} T_1 + (N+1)(N+2)\zeta_k^{-N-3} T_2 = \dfrac{\omega''(\zeta_k)}{R} - \sum_{n=1}^{N} n(n-1) a_n \zeta_k^{-n-1} \end{cases} \tag{C.2}$$

The truncated mapping function is in the form of

$$\begin{aligned}\omega_T(\zeta_k) &= R\left(\zeta_k + \sum_{n=1}^{N} a_n \zeta_k^{1-n} + T_1\zeta_k^{-n} + T_2\zeta_k^{-n-1}\right)\\ &= R\left(\zeta + \sum_{n=1}^{N+2} w_n \zeta_k^{1-n}\right)\end{aligned} \tag{C.3}$$

The complex function $\varphi(\zeta)$ at the kth tip of the M-branched crack with free surface is given as:

$$\varphi(\zeta_k) = \Gamma_1 R\zeta_k + \sum_{n=1}^{\infty} p_n \zeta_k^{1-n} \tag{C.4}$$

and the first $N+2$ coefficients p_n are obtained by solving

$$p_n + \sum_{k=1}^{N+2-n} (1-k)\overline{w_k} p_{n+k} + \sum_{k=1}^{N+2-n} (1-k) w_{n+k}\overline{p_k} + \Gamma_1 R w_n = \begin{cases} \overline{\Gamma_2} R; & n=2 \\ 0; & n \neq 2 \end{cases} \tag{C.5}$$

Let $p_n = p_n^R + ip_n^I$ and $w_n = w_n^R + iw_n^I$, Eq. (C.5) become a $(2N+4)$-order linear equations. In its compact form, we have

$$\mathbf{W}\boldsymbol{p} = \boldsymbol{b} \tag{C.6}$$

where $(2N+4)$-order vector $\boldsymbol{p}$ and $\boldsymbol{b}$ are in the form of $\boldsymbol{p} = [p_1^R, \dots, p_{N+2}^R, p_1^I, \dots, p_{N+2}^I]^{\mathrm{T}}$ and $\boldsymbol{b} = -[\Gamma_1 R w_1^R, \dots, \Gamma_1 R w_{N+2}^R, \Gamma_1 R w_1^I, \dots, \Gamma_1 R w_{N+2}^I]^{\mathrm{T}} + [0, \Re(\Gamma_2)R, \dots, 0, 0, \Im(\Gamma_2)R, \dots, 0]^{\mathrm{T}}$, respectively. $\Re(\cdot)$ and $\Im(\cdot)$ denote the real and imaginary part of $(\cdot)$, respectively. $\mathbf{W}$ is a $(2N+4)$-order matrix in the form of

$$\mathbf{W} = \begin{bmatrix} \mathbf{I} & \mathbf{0} \\ \mathbf{0} & \mathbf{I} \end{bmatrix} + \begin{bmatrix} \Re(\mathbf{W}_1) & \Im(\mathbf{W}_1) \\ -\Im(\mathbf{W}_1) & \Re(\mathbf{W}_1) \end{bmatrix} + \begin{bmatrix} \Re(\mathbf{W}_2) & \Im(\mathbf{W}_2) \\ \Im(\mathbf{W}_2) & -\Re(\mathbf{W}_2) \end{bmatrix} \tag{C.7}$$

where $\mathbf{I}$, $\mathbf{0}$, $\mathbf{W}_1$ and $\mathbf{W}_2$ are $(N+2)$-order matrices. $\mathbf{I}$ is an identity matrix and $\mathbf{0}$ is a zero matrix. $\mathbf{W}_1$ and $\mathbf{W}_2$ are in the form of

$$\mathrm{W}_1(n,k) = \begin{cases} (1-k+n)w_{k-n}, & k-n>0 \\ 0, & k-n\le 0 \end{cases} \tag{C.8a}$$

and

$$\mathrm{W}_2(n,k) = \begin{cases} (1-k-n)w_{k+n}, & k+n \le N+2 \\ 0, & k+n > N+2 \end{cases} \tag{C.8b}$$

where $n,k = 1,2,\dots,N+2$, and $\mathrm{W}_j(n,k)$ means the element at the nth line and kth column in $\mathbf{W}_j$, $j=1,2$.

With all the coefficients in Eq. (C.5) known, we may calculate the SIFs at the kth tip in the form of

$$K = K_{\mathrm{I}} - iK_{\mathrm{II}} = \frac{2\sqrt{\pi}\varphi'(\zeta_k)}{\sqrt{\omega''(\zeta_k)\mathrm{e}^{i\delta_k}}} \tag{C.9}$$

where $\delta_k = \sum_{j=1}^{k-1}\theta_j$. By repeating the above steps, we obtain the SIFs and hence the strain energy release rate at all tips of a branched crack.

References

Adda-Bedia, M., 2005. Brittle fracture dynamics with arbitrary paths III. The branching instability under general loading. J. Mech. Phys. Solids 53 (1), 227–248. http://dx.doi.org/10.1016/j.jmps.2004.06.001.

Amestoy, M., Leblond, J., 1992. Crack paths in plane situations—II. Detailed form of the expansion of the stress intensity factors. Int. J. Solids Struct. 29 (4), 465–501. http://dx.doi.org/10.1016/0020-7683(92)90210-K.

Andersson, H., 1969. Stress-intensity factors at the tips of a star-shaped contour in an infinite tensile sheet. J. Mech. Phys. Solids 17 (5), 405–406. http://dx.doi.org/10.1016/0022-5096(69)90026-X.

Bilby, B.A., Cardew, G.E., 1975. The crack with a kinked tip. Int. J. Fract. 11 (4), 708–712. http://dx.doi.org/10.1007/BF00116380.

Bilby, B., Cardew, G., Howard, I., 1977. Stress intensity factors at the tips of kinked and forked cracks. In: Taplin, D. (Ed.), Analysis and Mechanics. Pergamon, pp. 197–200. http://dx.doi.org/10.1016/B978-0-08-022142-7.50039-9.

Bowie, O.L., 1964. Rectangular Tensile Sheet With Symmetric Edge Cracks. J. Appl. Mech. 31 (2), 208–212. http://dx.doi.org/10.1115/1.3629588.

Brown, J.W., Churchill, R.V., 2009. Complex Variables and Applications, eighth ed. McGraw-Hill Higher Education.

Buehler, M.J., Gao, H., 2006. Dynamical fracture instabilities due to local hyperelasticity at crack tips. Nature 439 (7074), 307–310. http://dx.doi.org/10.1038/nature04408.

Burghard, Z., Zimmermann, A., Rödel, J., Aldinger, F., Lawn, B.R., 2004. Crack opening profiles of indentation cracks in normal and anomalous glasses. Acta Mater. 52 (2), 293–297. http://dx.doi.org/10.1016/j.actamat.2003.09.014.

Chatterjee, S.N., 1975. The stress field in the neighborhood of a branched crack in an infinite elastic sheet. Int. J. Solids Struct. 11 (5), 521–538. http://dx.doi.org/10.1016/0020-7683(75)90027-X.

Chen, Y.Z., Lin, X.Y., Wang, Z.X., 2009. A singular integral equation method for examining asymptotic solutions of a kinked crack with infinitesimal kink length. J. Mech. Mater. Struct. 4 (11), 1657–1674. http://dx.doi.org/10.2140/jomms.2009.4.1657.

Cheng, H., Zhou, X., 2020. An energy-based criterion of crack branching and its application on the multidimensional space method. Int. J. Solids Struct. 182–183, 179–192. http://dx.doi.org/10.1016/j.ijsolstr.2019.08.019.

Cotterell, B., Rice, J.R., 1980. Slightly curved or kinked cracks. Int. J. Fract. 16 (2), 155–169. http://dx.doi.org/10.1007/BF00012619.
Dönmez, A., Bažant, Z.P., 2020. Size effect on branched sideways cracks in orthotropic fiber composites. Int. J. Fract. 222 (1), 155–169. http://dx.doi.org/10.1007/s10704-020-00439-1.
Fayyad, T.M., Lees, J.M., 2017. Experimental investigation of crack propagation and crack branching in lightly reinforced concrete beams using digital image correlation. Eng. Fract. Mech. 182, 487–505. http://dx.doi.org/10.1016/j.engfracmech.2017.04.051.
Ferney, B., DeVary, M., Hsia, K., Needleman, A., 1999. Oscillatory crack growth in glass. Scr. Mater. 41 (3), 275–281. http://dx.doi.org/10.1016/S1359-6462(99)00161-X.
Hakimzadeh, M., Agrawal, V., Dayal, K., Mora-Corral, C., 2022. Phase-field finite deformation fracture with an effective energy for regularized crack face contact. J. Mech. Phys. Solids 167, 104994. http://dx.doi.org/10.1016/j.jmps.2022.104994.
Hayashi, K., Nemat-Nasser, S., 1981. Energy-release rate and crack kinking under combined loading. J. Appl. Mech. 48 (3), 520–524. http://dx.doi.org/10.1115/1.3157666.
He, M.-Y., Bartlett, A., Evans, A.G., Hutchinson, J.W., 1991. Kinking of a crack out of an interface: Role of in-plane stress. J. Am. Ceram. Soc. 74 (4), 767–771. http://dx.doi.org/10.1111/j.1151-2916.1991.tb06922.x.
He, M.Y., Hutchinson, J.W., 1989. Crack deflection at an interface between dissimilar elastic materials. Int. J. Solids Struct. 25 (9), 1053–1067. http://dx.doi.org/10.1016/0020-7683(89)90021-8.
Hussain, M., Pu, S., Underwood, J., 1973. Strain energy release rate for a crack under combined mode I and mode II. In: Proceedings of the 1973 National Symposium on Fracture Mechanics. ASTM Inrernational, pp. 2–28.
Hutchinson, J.W., Mear, M.E., Rice, J.R., 1987. Crack paralleling an interface between dissimilar materials. J. Appl. Mech. 54 (4), 828–832. http://dx.doi.org/10.1115/1.3173124.
Irwin, G.R., 1957. Analysis of stresses and strains near the end of a crack traversing a plates. J. Appl. Mech. 29, 63–191. http://dx.doi.org/10.1115/1.4011547.
Karihaloo, B.L., Keer, L.M., Nemat-Nasser, S., Oranratnachai, A., 1981. Approximate description of crack kinking and curving. J. Appl. Mech. 48 (3), 515–519. http://dx.doi.org/10.1115/1.3157665.
Katzav, E., Adda-Bedia, M., Arias, R., 2007. Theory of dynamic crack branching in brittle materials. Int. J. Fract. 143 (3), 245–271. http://dx.doi.org/10.1007/s10704-007-9061-x.
Leblond, J.-B., Karma, A., Ponson, L., Vasudevan, A., 2019. Configurational stability of a crack propagating in a material with mode-dependent fracture energy - Part I: Mixed-mode I+III. J. Mech. Phys. Solids 126, 187–203. http://dx.doi.org/10.1016/j.jmps.2019.02.007.
Li, W., Frash, L.P., Lei, Z., Carey, J.W., Chau, V.T., Rougier, E., Meng, M., Karra, S., Nguyen, H.T., Rahimi-Aghdam, S., Bažant, Z.P., Viswanathan, H., 2022. Investigating poromechanical causes for hydraulic fracture complexity using a 3D coupled hydro-mechanical model. J. Mech. Phys. Solids 169, 105062. http://dx.doi.org/10.1016/j.jmps.2022.105062.
Liu, X., Athanasiou, C.E., Padture, N.P., Sheldon, B.W., Gao, H., 2020. A machine learning approach to fracture mechanics problems. Acta Mater. 190, 105–112. http://dx.doi.org/10.1016/j.actamat.2020.03.016.
Liu, Z.-E., Wei, Y., 2021. An analytical solution to the stress fields of kinked cracks. J. Mech. Phys. Solids 156, 104619. http://dx.doi.org/10.1016/j.jmps.2021.104619.
Lo, K.K., 1978. Analysis of branched cracks. J. Appl. Mech. 45 (4), 797–802. http://dx.doi.org/10.1115/1.3424421.
Muskhelishvili, N.I., 1953. Some Basic Problems of the Mathematical Theory of Elasticity. Noordhoff.
Rice, J.R., 1968. A path independent integral and the approximate analysis of strain concentration by notches and cracks. J. Appl. Mech. 35 (2), 379–386. http://dx.doi.org/10.1115/1.3601206.
Rice, J.R., 1972. Some remarks on elastic crack-tip stress fields. Int. J. Solids Struct. 8 (6), 751–758. http://dx.doi.org/10.1016/0020-7683(72)90040-6.
Ruan, L., Luo, R., Wang, B., Yu, X., 2021. Morphological characteristics of crack branching in asphalt mixtures under compression. Eng. Fract. Mech. 253, 107884. http://dx.doi.org/10.1016/j.engfracmech.2021.107884.
Salvadori, A., Fantoni, F., 2016. Fracture propagation in brittle materials as a standard dissipative process: General theorems and crack tracking algorithms. J. Mech. Phys. Solids 95, 681–696. http://dx.doi.org/10.1016/j.jmps.2016.04.034.
Sharon, E., Fineberg, J., 1996. Microbranching instability and the dynamic fracture of brittle materials. Phys. Rev. B 54 (10), 7128–7139. http://dx.doi.org/10.1103/PhysRevB.54.7128.
Sharon, E., Fineberg, J., 1999. Confirming the continuum theory of dynamic brittle fracture for fast cracks. Nature 397 (6717), 333–335. http://dx.doi.org/10.1038/16891.
Sumi, Y., Nemat-Nasser, S., Keer, L.M., 1983. On crack branching and curving in a finite body. Int. J. Fract. 21 (1), 67–79. http://dx.doi.org/10.1007/BF01134200.
Sundaram, B.M., Tippur, H.V., 2016. Dynamics of crack penetration vs. Branching at a weak interface: An experimental study. J. Mech. Phys. Solids 96, 312–332. http://dx.doi.org/10.1016/j.jmps.2016.07.020.
Sundaram, B.M., Tippur, H.V., 2018. Dynamic fracture of soda-lime glass: A full-field optical investigation of crack initiation, propagation and branching. J. Mech. Phys. Solids 120, 132–153. http://dx.doi.org/10.1016/j.jmps.2018.04.010.
Vattré, A., 2022. Kinked and forked crack arrays in anisotropic elastic bimaterials. J. Mech. Phys. Solids 160, 104744. http://dx.doi.org/10.1016/j.jmps.2021.104744.
Williams, M.L., 1957. On the stress distribution at the base of a stationary crack. J. Appl. Mech. 24 (1), 109–114. http://dx.doi.org/10.1115/1.4011454.
Wu, C.H., 1978. Elasticity problems of a slender Z-crack. J. Elasticity 8 (2), 183–205. http://dx.doi.org/10.1007/BF00052482.
Wu, C.H., 1979. Explicit asymptotic solution for the maximum-energy-release-rate problem. Int. J. Solids Struct. 15 (7), 561–566. http://dx.doi.org/10.1016/0020-7683(79)90083-0.
Xu, R.L., Huang, Y., Rosakis, A.J., 2003. Dynamic crack deflection and penetration at interfaces in homogeneous materials: Experimental studies and model predictions. J. Mech. Phys. Solids 51 (3), 461–486. http://dx.doi.org/10.1016/S0022-5096(02)00080-7.
Zeng, X., Wei, Y., 2017. Crack deflection in brittle media with heterogeneous interfaces and its application in shale fracking. J. Mech. Phys. Solids 101, 235–249. http://dx.doi.org/10.1016/j.jmps.2016.12.012.
Zhang, X., Dunne, F.P., 2022. 3D CP-XFEM modelling of short crack propagation interacting with twist/tilt nickel grain boundaries. J. Mech. Phys. Solids 168, 105028. http://dx.doi.org/10.1016/j.jmps.2022.105028.